Nuclear Medicine and Biology 84–85 (2020) 102–110

Contents lists available at ScienceDirect

Nuclear Medicine and Biology

journal homepage: www.elsevier.com/locate/nucmedbio

Preparation and in vivo evaluation of red blood cell membrane coated porous silicon nanoparticles implanted with ^{155}Tb

Ulrika Jakobsson [a,b], Ermei Mäkilä [c], Antti Rahikkala [d], Surachet Imlimthan [a], Jarkko Lampuoti [a], Sanjeev Ranjan [a,h], Jouni Heino [b], Pasi Jalkanen [e], Ulli Köster [f], Kenichiro Mizohata [e], Hélder A. Santos [d,g], Jarno Salonen [c], Anu J. Airaksinen [a,i], Mirkka Sarparanta [a,*], Kerttuli Helariutta [a,b,*]

[a] Department of Chemistry, University of Helsinki, Finland
[b] Helsinki Institute of Physics, University of Helsinki, Finland
[c] Department of Physics and Astronomy, University of Turku, Finland
[d] Drug Research Program, Division of Pharmaceutical Chemistry and Technology, Faculty of Pharmacy, University of Helsinki, Finland
[e] Department of Physics, University of Helsinki, Finland
[f] Institut Laue-Langevin, Grenoble, France
[g] Helsinki Institute of Life Science (HiLIFE), University of Helsinki, Finland
[h] Institute of Biomedicine, University of Eastern Finland, Kuopio, Finland
[i] Turku PET Centre, University of Turku, Finland

ARTICLE INFO

Article history:
Received 1 October 2019
Received in revised form 3 April 2020
Accepted 5 April 2020

Keywords:
Terbium-155
Radioactive ion beam
Porous silicon
Red blood cell membrane
Circulation time
Theranostics

ABSTRACT

Introduction: Porous silicon (PSi) nanoparticles are capable of delivering therapeutic payloads providing targeted delivery and sustained release of the payloads. In this work we describe the development and proof-of-concept *in vivo* evaluation of thermally hydrocarbonized porous silicon (PSi) nanoparticles that are implanted with radioactive ^{155}Tb atoms and coated with red blood cell (RBC) membrane (^{155}Tb-THCPSi). The developed nanocomposites can be utilized as an intravenous delivery platform for theranostic radionuclides.
Methods: THCPSi thin films were implanted with ^{155}Dy ions that decay to ^{155}Tb at the ISOLDE radioactive ion-beam (RIB) facility at CERN. The films were processed to nanoparticles by ball-milling and sonication, and subsequently coated with either a solid lipid and RBC membrane or solely with RBC membrane. The nanocomposites were evaluated *in vitro* for stability and *in vivo* for circulation half-life and *ex vivo* for biodistribution in Balb/c mice.
Results: Nanoporous THCPSi films were successfully implanted with ^{155}Tb and processed to coated nanoparticles. The *in vitro* stability of the particles in plasma and buffer solutions was not significantly different between the particle types, and therefore the RBC membrane coated particles with less laborious processing method were chosen for the biological evaluation. The RBC membrane coating enhanced significantly the blood half-life compared to bare THCPSi particles. In the *ex vivo* biodistribution study a pronounced accumulation to the spleen was found, with lower uptake in the liver and a minor uptake in the lung, gall bladder and bone marrow.
Conclusions: We have demonstrated, using ^{155}Tb RIB-implanted PSi nanoparticles coated with mouse RBC membranes, the feasibility of using such a theranostic nanosystem for the delivery of RIB based radionuclides with prolonged circulation time.
Advances in knowledge and implications for patient care: For the first time, the RIB implantation technique has been utilized to produce PSi nanoparticle with a surface modified for better persistence in circulation. When optimized, these particles could be used in targeted radionuclide therapy with a combination of chemotherapeutic payload within the PSi structure.

1. Introduction

Porous silicon (PSi) has gained over the past two decades widespread interest as a nanoscale drug delivery system due to its capability to deliver a multitude of poorly soluble therapeutics [1–4], biological drugs [5–8] and even secondary nanomaterial payloads [9], providing enhanced biological barrier permeation, targeted delivery and sustained

* Corresponding authors at: Department of Chemistry, P.O.Box 55 (A.I. Virtasen aukio 1), FI-00014 University of Helsinki, Finland.
E-mail addresses: mirkka.sarparanta@helsinki.fi (M. Sarparanta), kerttuli.helariutta@helsinki.fi (K. Helariutta).

https://doi.org/10.1016/j.nucmedbio.2020.04.001

release. It has demonstrated high biocompatibility and safety [10–13] in all administration routes with biodegradation into silicic acid excreted in urine for facile elimination from the body [14,15]. Fabrication of porous silicon can be done using various top-down and bottom-up approaches which provide a wide selection of pore morphologies and structures depending on the method [16]. A common method of fabrication is through electrochemical anodization of crystalline silicon wafers in aqueous hydrofluoric acid (HF) solutions where the porosity, pore size and thickness of the porous layer can be easily controlled by the composition of the etching media and the applied anodization current [17]. Recently, bottom-up synthetic approaches resulting in PSi nanoparticles of a controlled spherical geometry have been reported, and biomedical applications such as drug delivery and immunotherapy employing spherical nanoparticles produced using the high-shear microfluidization techniques are becoming prevalent over the ones using quasi-spherical particles produced by ultrasonication [18]. The freshly-etched, or "as-anodized" surface of PSi is highly reactive due to the presence of surface hydrides [19], and consequently, subsequent chemical modification is warranted to stabilize the surface and to provide functional handles for further surface modification to tailor the drug delivery properties [20,21] and for the conjugation of imaging labels [1,10,22,23] and targeting moieties [24–26]. The surface modifications used for the passivation and functionalization of the fresh, hydrogen-terminated PSi surface include thermal oxidation [27], thermal carbonization and thermal hydrocarbonization [28,29], and various techniques of hydrosilylation providing an avenue to for example carboxylic acid, amine, and alkyne terminated PSi [30–32]. The modification of interest for this work is thermal hydrocarbonization, which renders the PSi surface hydrophobic and amenable to subsequent encapsulation for example into a solid lipid nanoparticle for tailoring of the degradation kinetics [33], or into isolated mouse red blood cell membrane for evasion of immune recognition and prolonged residence in circulation [34].

Nanoscale drug delivery systems are intensely investigated for improving the effectiveness and safety of drug therapy in cancer. However, many nanosystems fail to provide significant therapeutic advantage due to suboptimal *in vivo* performance including short circulation time, immune recognition, and poor tumor accumulation and penetration [35]. There has been increasing interest in new technologies to prolong nanoparticle circulation time in human body, with polymer encapsulation (typically PEGylation), liposomal drug carriers and serum albumin conjugates being the most widely applied and clinically translated [36]. Recently however, cell membrane-derived drug carriers have emerged as natural, biocompatible, and long-circulating options for drug delivery and immunotherapy [37,38]. Red blood cells (RBC) express on their surface CD47, which is a trans-membrane protein signaling to macrophages not to phagocytose them [39]. RBC-membrane camouflaged nanoparticles (NP) have demonstrated to possess a significantly improved capability for evasion from the mononuclear phagocytic system (MPS) recognition compared to the current gold standard of PEGylated NPs. Furthermore, even though PEGylation results in an extended NP circulation time initially, a second injection of the same formulation often leads to much more rapid clearance compared to the first injection due to an immune response to the PEGylated particles [40].

The use of theranostic matched isotopic multiplets has gained increasing interest in radiotherapy. A theranostic multiplet consists of one element having isotopes with different medically relevant radiative properties. One prominent example is the theranostic quadruplet of terbium [41], where the isotopes ^{152}Tb (β^+, $t_{1/2} = 17.5$ h) and ^{155}Tb (EC, $t_{1/2} = 5.32$ d) are suitable for imaging (positron emission tomography (PET) and single photon emission computed tomography (SPECT), respectively) and the isotopes ^{149}Tb (α/β^+, $t_{1/2} = 4.12$ h) and ^{161}Tb (β^-, $t_{1/2} = 6.89$ d) have a potential to be used for therapy (through alpha and beta/CE/Auger electron emission, respectively) [42]. Neutron-rich ^{161}Tb is produced by irradiation of enriched ^{160}Gd targets in high flux reactors. Short-lived ^{161}Gd produced by thermal neutron capture decays quickly ($T_{1/2} = 3.6$ min) to ^{161}Tb. Subsequently, n.c.a. ^{161}Tb is radiochemically separated from the Gd targets [43,44]. Similar to commercially available n.c.a. ^{177}Lu this method can be upscaled to TBq activities per batch. On the other hand, the neutron-deficient Tb isotopes were so far mainly produced by GeV proton induced spallation reactions combined with on-line mass separation at the ISOLDE facility at CERN [45] and collected as radioactive ion beams (RIB), a method also used here and described in more detail in Section 2.2. Now a dedicated facility, MEDICIS at CERN [46], is under commissioning to make these isotopes available more frequently. Production of ^{152}Tb and ^{155}Tb can also be envisaged by (p,n) reactions at medical cyclotrons combined with a radiochemical Tb/Gd separation (similar to n.c.a. ^{161}Tb production), provided sufficiently enriched ^{152}Gd and ^{155}Gd targets become available [47].

Previously, we have demonstrated thermally hydrocarbonized porous silicon (THCPSi) as a suitable platform for implantation of RIB-based radiolantanoids using ^{159}Dy [48]. Herein, we describe the development and proof-of-concept *in vivo* evaluation of thermally hydrocarbonized PSi nanoparticles that are implanted with radioactive ^{155}Tb atoms and coated with RBC membrane as an intravenous delivery platform for the theranostic quadruplet of terbium, as well as for other RIB based nuclei. In contrast to conventional radiolabeling methods, the RIB implantation process is independent on the chemistry of the radionuclide, and therefore the radiolabel can be easily changed to any radionuclide that can be obtained from a RIB facility. To this end, PSi offers several advantages including the possibility for RIB implantation into free-standing films which can be post-processed to nanoparticles, the possibility to add a secondary chemotherapeutic payload to the porous network of PSi, as well as the targeting and stealth capability endowed by the RBC encapsulation. THCPSi free-standing films were implanted with a radioactive ion beam of ^{155}Tb at the ISOLDE beam line at CERN, postprocessed to radiolabeled nanoparticles, and coated with Balb/c mouse RBC membranes with and without a solid lipid (glyceryl monostearate/L-α-phosphatidyl choline/polyvinyl alcohol/PEG) coating prepared using a solid-in-oil-in-water (S/O/W) emulsion method. We report the *in vitro* stability of the ^{155}Tb-nanocomposites in physiological media with the determination of the circulation half-life and *ex vivo* biodistribution after a single intravenous administration to healthy female Balb/c mice.

2. Experimental

2.1. Production of THCPSi

The THCPSi thin films were fabricated by electrochemically anodizing boron-doped p^+-type Si(100) wafers of 0.01–0.02 Ωcm resistivity in a 1:1 (*v*/v) HF (38%)–ethanol electrolyte using a pulsed etching profile, producing alternating high and low porosity layers. After the total thickness of the porous layer had reached *ca.* 40 μm, the layer was lifted off the wafer by increasing the etching current into electropolishing region. The obtained multilayer PSi thin films were then thermally hydrocarbonized at 500 °C with acetylene using a previously described method [21].

2.2. Radionuclide implantation and depth profile

Two 40-μm thick THCPSi films (∅ = 1 cm) were implanted at the ISOLDE ion-beam facility at CERN with ^{155}Dy ions that decay ($t_{1/2} = 9.9$ h) to ^{155}Tb. A 1.4 GeV proton beam impinged on a primary tantalum target. Radioactive lanthanoid nuclides were produced in the tantalum foil target (94 g/cm^2 Ta) through spallation reactions, thermally released from the 2000 °C hot target, ionized in a 2000 °C hot tungsten cavity, accelerated with a voltage of 30 kV and mass-separated with the magnetic sector field of the ISOLDE General Purpose Separator [49]. The thermal ionization of dysprosium was significantly enhanced with the resonance ionization laser ion source [50,51] tuned to

dysprosium, yielding a radioactive ion beam of ^{155}Dy with an intensity of about 10^{10} particles per second. Two THCPSi films were mounted on iron holders and placed in a collection chamber on the high-mass side of the general-purpose separator. ^{155}Dy ions were implanted into the mesoporous layer one film after another over a time of 85 and 45 min, respectively. The samples were implanted also with ^{139}Ce (EC, $t_{1/2} = 137.6$ d) as an impurity, resulting as a molecular side band from the primary target.

To characterize the implantation process, a separate run at ISOLDE was performed in order to estimate the implantation depth of the parent activity ^{155}Dy. A beam of ^{155}Dy with an energy of 50 keV was implanted into a 40-μm thick THCPSi film. After that, the film was exposed to a successive ion-beam etching to remove layers of material from the top of the film and deposit them on a moving tape. Altogether 30 tape samples were produced by etching, first ten in 10 nm steps, next ten in 50 nm steps and last ten in 1 μm steps. The tape was sectioned and from each section a gamma-ray intensity was measured using a Hidex Automatic Gamma Counter with the energy window set at the characteristic gamma-ray peak of the daughter activity ^{155}Tb. For calibrating the total depth reached by the etching process, a profilometer (KLA-Tencorin P-15) was used. In order to understand the depth profile of the sputtering results, the profile was simulated using SRIM – The Stopping and Range of Ions in Matter software package [52]. The penetration of 30 keV ^{155}Dy ions was simulated in solid and in 70% porous silicon, resulting in the depth profiles of ^{155}Dy in the simulated materials.

It has to be stressed that in the present method the primary production target and the secondary implantation target are completely separate. The production target (here tantalum) is irradiated by GeV proton beams to induce spallation reactions and is located in a heavily shielded area. In contrast the implantation target (here THCPSi film) is easily accessible in a dedicated vacuum chamber where it gets ion-implanted with a mass-separated low-energy radioactive ion beam. Hence, type and geometry of either target can be chosen and optimized completely independently which gives this method a particular flexibility. Unlike other radiolabeling methods where the sample itself is activated by neutron or charged particle irradiation here only the radioisotope of interest or possible (pseudo-)isobars are implanted but no other disturbing radionuclides are generated during the implantation (heavy ions of 30 keV are far too slow to overcome the Coulomb barrier; several orders of magnitude higher energies would be required to induce nuclear reactions).

2.3. Irradiation post-processing

The implanted films were transported to the University of Helsinki for post-implantation processing. The activity of the films was first measured by using a HPGe detector. After that, the films were extracted from the holders and placed into a small glass ampoule with 1 mm ZrO_2 beads. To enhance the milling process, a piece of inactive THCPSi film was added to the ampoule. The ampoule was filled with dec-1-ene and milled with a planetary ball mill (Fritsch Pulverisette 6) using an in-house made adapter. After milling, the milled slurry of THCPSi in dec-1-ene was sonicated with a tip sonicator (tip ∅ = 3 mm, QSonica, Newtown, CT, USA). After that, the dec-1-ene was replaced with ethanol using centrifugation. Particle size selection was done by centrifugation in ethanol dispersions.

A reference batch of inactive THCPSi nanoparticles was made using the same methods from non-implanted THCPSi films for physical characterization of the produced nanoparticles. Specific surface area and pore volume were calculated from results of nitrogen sorption at −196 °C (Tristar 3000, Micromeritics Inc., Norcross, USA) using the Brunauer-Emmett-Teller (BET) method and taking the total adsorbed amount of N_2 at a relative pressure (p/p_0) of 0.95. The porous structure was imaged with scanning electron microscopy using a field-emission SEM (Apreo S, Thermo Scientific, Eindhoven, The Netherlands). High-angle annular dark-field (HAADF) images were taken using a STEM detector attached to the field-emission SEM. Inactive coated nanoparticle samples were imaged using transmission electron microscopy (TEM, JEM-1400, JEOL, Tokyo, Japan), which was operated at 80 kV in a bright-field mode. The hydrodynamic diameter (*Z*-average) and polydispersity index (PdI) were measured in ethanol by dynamic light scattering (DLS) using a Malvern Zetasizer Nano ZS instrument (Malvern Panalytical, Malvern, UK). The role of DLS was to provide rapid size class information during the formulation process. The same instrument was used to measure the zeta potential of the nanoparticles in 10 mM phosphate-buffered saline (PBS), pH 7.4 based on electrophoretic mobility of the nanoparticles.

2.3.1. Solid lipid coating

The solid lipid (SL) coating of [^{155}Tb]THCPSi nanoparticles was carried out using a solid-in-oil-in-water (S/O/W) emulsion method as reported previously for fluorine-18 -radiolabeled THCPSi [53]. Briefly, the nanoparticles, glyceryl monostearate (100 mg) and L-α-phosphatidyl choline (40 mg) were dispersed in 5 ml ethanol at 70 °C forming the oil phase containing solid dispersion (S/O). After 5 min, the nanoparticle solution was added dropwise under vigorous stirring to 15 ml of heated (70 °C) solution of 1% (*w*/*v*) PVA (31–50 kDa) and 1% (w/v) PEG (6 kDa) over 30 min to form the emulsion. The emulsion was stirred for 10 min and added gradually using air flow to a cooled aqueous solution of 1% PVA and PEG (25 ml, 2 °C ice bath) to allow the hardening of the lipid matrix. The final suspension was stirred on ice for further 15 min, and the solid lipid -coated [^{155}Tb]THCPSi-SL were separated from the solution by centrifugation. Finally [^{155}Tb]THCPSi-SL were sonicated in 0.3% Tween 80 (*w*/*v*) for 90 s with 5 s pulse every 30 s. Thereafter, the final solution of [^{155}Tb]THCPSi-SL was moved to the next step of RBC membrane coating.

2.3.2. RBC membrane coating

Whole blood (5.5 ml, withdrawn from five 12-week old Balb/c female mice as will be described in Section 2.5) was diluted with 5.5 ml phosphate-buffered saline (PBS) at pH 7.4. The diluted blood was layered atop 3 ml of Ficoll-Paque medium in a 15 ml centrifuge tube and centrifuged for 40 min at 400 *g*. After the centrifugation, the RBCs were collected from the bottom of the centrifuge tube. The RBCs were then washed four times with PBS by centrifugation at 4020 *g*. The final RBC yield was $\approx 9 \times 10^5$ cells/ml. Then, the RBCs were resuspended in 2 ml lysis buffer (20 mM Tris-HCl pH 7.5, 10 mM KCl, 2 mM $MgCl_2$ in milli-Q water). After a brief ultrasonication, the solution was centrifuged at 4020 *g* and the supernatant collected. The pellet was resuspended in 2 ml of lysis buffer, centrifuged again at 4020 *g*, and the supernatant was collected and pooled together with the first supernatant. Then, the supernatant was centrifuged at 20,000 *g* for 20 min at 4 °C using a TLA 120.2 rotor in an Optima MAX ultracentrifuge (Beckmann Coulter, USA). The pellet was discarded and the supernatant was finally centrifuged at 100,000 *g* for 5 min at 4 °C. The resulting pellet was re-dispersed in 5.5 ml of milli-Q water.

The RBC coating procedure was first optimized in terms of the extruder membrane pore diameter using the non-radioactive reference THCPSi and THCPSi-SL nanoparticles. After optimization, the 400-nm pore size was determined to be optimal, and was used in the RBC coating procedure for the [^{155}Tb]THCPSi and [^{155}Tb]THCPSi-SL nanoparticles as follows: 360 μg of either [^{155}Tb]THCPSi or [^{155}Tb]THCPSi-SL in 300 μl of 0.3%(*v*/v) Tween 80–1 × PBS, pH = 7.4, was divided into two 1.5-ml microtubes. Then, 500 μl of RBC membranes in milli-Q water and 350 μl buffer was added in both the tubes to have a total volume of 2 × 1 ml. The 1 ml samples were separately extruded 21 times across a semi-permeable membrane with 400-nm pore size (Avanti Polar Lipids, Alabaster, AL, USA) using a mini-extruder with 1 ml syringe volume (Avanti Polar Lipids). The needed number of extrusions was obtained by analyzing TEM images of samples after different number of extrusions during the development phase of the extrusion process.

2.4. In vitro radiolabel stability assay

For the selection of the optimal nanoparticle design for the *in vivo* experiment, an *in vitro* radiolabel dissolution test for the particles was carried out. 10 μl, 30 μl and 50 μl of [^{155}Tb]THCPSi, [^{155}Tb]THCPSi-RBC and [^{155}Tb]THCPSi-SL-RBC suspensions, respectively, were placed to 50-ml conical polypropylene centrifuge tubes with 30 ml of three different solutions: two phosphate-buffered saline (PBS) solutions with physiologically relevant pHs 7.4 and 5.6, and a mixture of 50% pH 7.4 PBS and 50% human plasma (from the Finnish Red Cross Blood Service, Helsinki, Finland). All experiments were carried out in triplicate and the radioactivity concentration (not NP concentration due to the different specific activity of each nanoparticle type) was kept constant across all samples. The vials were incubated at 37 °C under constant shaking. A 450-μl sample was taken from each vial at 30 min, 1 h, 4 h, 8 h, 20 h, 40 h and 60 h for all samples and additional two samples at 156 h and 228 h were taken for the pH 7.4 and pH 5.6 vials. At each sampling, the withdrawn sample volume was replaced with respective amount of buffer solution. The samples (450 μl) were taken into 0.5-ml centrifugal filter devices with a 10-kDa MWCO poly(ethersulfone) (PES) membrane (VWR Collection), and the particles were separated from the solution by centrifugation (13,000 *g* for 15 min). Both particles and solution were measured with Hidex Automatic Gamma Counter (Hidex Corporation, Turku, Finland), and the percentage of undissolved activity in particles was calculated, with correction for the inactive buffer solution added to each sample.

2.5. RBC membrane isolation and in vivo determination of [^{155}Tb]THCPSi-RBC nanoparticle circulation half-life in mice

All animal experiments were conducted under the ethical approval of the National Board for Animal Experimentation in Finland (license number ESAVI/12132/04.10.07/2017) and in accordance to the respective national and European guidelines and policies. 8-week old female Balb/cAnN:Crl mice used in all experimental procedures were purchased from Charles River (Scanbur A/S, Karlslunde, Denmark) and group-housed in conventional polycarbonate caging on aspen bedding in a HEPA-filtered environmentally controlled (temperature 22 ± 1 °C, 55 ± 10% relative humidity, 12:12 light cycle) housing unit. Rodent chow and water were provided *ad libitum*.

For red blood cell membrane isolation, the mice were anesthetized with an intraperitoneal injection of 100 mg/kg of sodium pentobarbital (Mebunat Vet 60 mg/ml, Orion Pharma, Espoo, Finland) and blood was collected with cardiac puncture to Na-citrate tubes (Greiner-Bio-One Vacuette Na-Citrate 3.2%, 1 part anticoagulant to 5 parts mouse whole blood) and stored on ice until RBC isolation.

The mice were administered intravenously 9.58 ± 0.08 kBq of [^{155}Tb]THCPSi-RBC nanoparticles in 0.3%(*v*/v) Tween 80–1 × PBS, pH = 7.4 using a 29G insulin syringe, and venous blood samples (10–20 μl) were collected to weighed 1.5-ml microtubes from the contralateral vein through a temporary cannula at 20 min, 1 h, 2 h and 4 h after administration followed by sacrifice with CO_2 asphyxiation and blood collection by cardiac puncture at 8 h after administration. The radioactivity in the blood samples (from 4 to 5 mice per time point) was measured on a gamma-ray spectrometer, and the results are expressed as percentage of injected dose per gram (%ID/g) of blood.

2.6. Ex vivo biodistribution of [^{155}Tb]THPSi-RBC in mice after intravenous injection

At 8 h post injection, the mice ($n = 5$) were euthanized by CO_2 asphyxiation and urine, blood and selected tissues were collected, weighed and the radioactivity measured using gamma ray spectrometry as described below. The results of the biodistribution are expressed as % ID/g of tissue.

2.7. Gamma ray spectrometry

The activities of the organ and blood samples were determined using Hidex Automatic Gamma Counter with a 3″ well-type NaI crystal. The measurement efficiency was determined using calibration standards whose activities were measured using an efficiency calibrated HPGe spectrometer (Ortec GEM-25195-P-S). The activities of the 4 and 8-h blood samples with the smallest activities were re-measured with an efficiency calibrated, sensitive Canberra GX8021 Xtra detector (relative efficiency 95.8%) for minimizing the detection limit.

3. Results and discussion

3.1. Depth profile of implanted radionuclides in PSi

The experimentally obtained depth profile of ^{155}Dy in a THCPSi film is shown in Fig. 1, together with the depth profiles simulated with SRIM package. The simulated depth distribution in solid silicon (indicated in purple) peaks at roughly 30 nm. The simulated distribution in a silicon with a porosity to 70% (indicated in green) yields a broader distribution peaking at depth of 100 nm, evident also through scaling. The experimental profile (indicated in blue) peaks at the same depth but the width does not correspond directly to that of the simulated one. This can be understood when considering the structure of a PSi film, shown in Fig. 2, where the surface and cross-sectional view of a THCPSi foil can be seen. The particles are implanted into a non-uniform, porous surface, allowing the ions randomly either to penetrate deeper in the material through a pore or stop faster in the branching solid silicon skeleton.

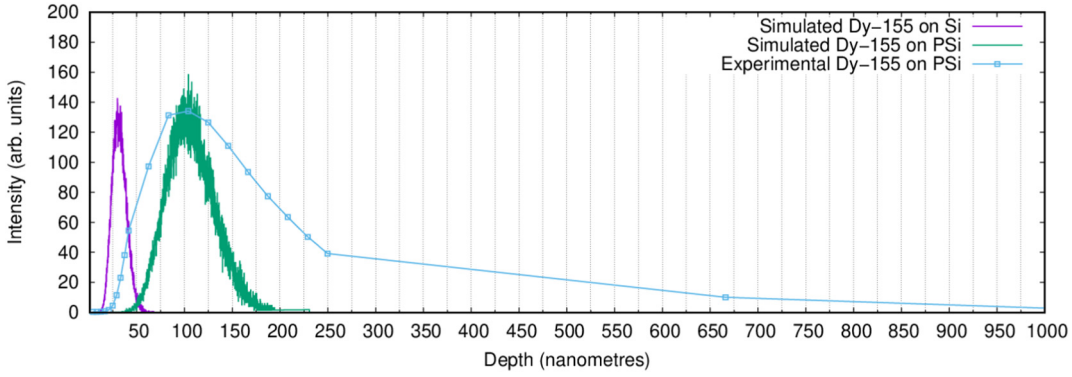

Fig. 1. Experimental depth profile of ^{155}Dy in THCPSi (blue dots). Simulated depth in solid silicon is depicted in purple and in silicon with 70% porosity in green.

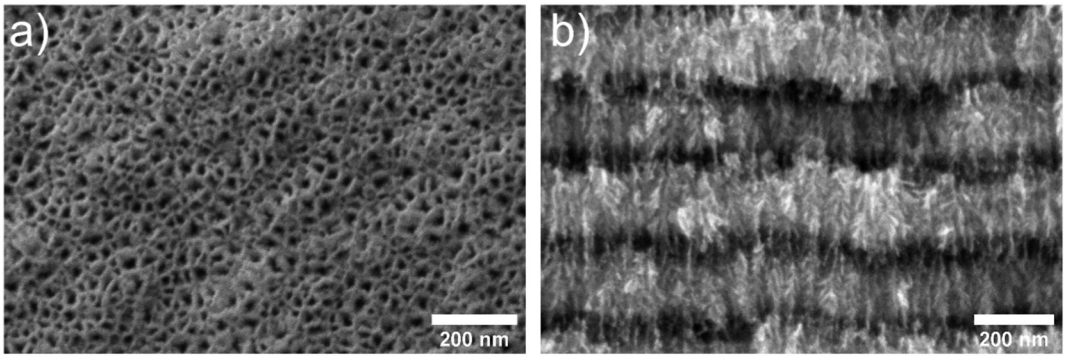

Fig. 2. A scanning electron microscope picture of the structure of a THCPSi film. a) Plan view of the pore openings in the surface of the film. b) Cross-section view of the porous silicon multilayer structure showing the alternating low and high porosity regions.

3.2. Irradiation post-processing

The THCPSi films arrived at University of Helsinki a little over four days after the implantation. At this time, the activities in the films were measured with at HPGe detector and were about 57 MBq for ^{155}Tb, 2.5 MBq for ^{155}Dy and 3.6 MBq for ^{139}Ce. The total mass of the silicon films in the beginning of the process was 17.4 mg of which 4.4 mg were covered by the ^{155}Dy implanted films and 13 mg by the added inactive film. The activity of ^{155}Tb was followed in all stages of particle processing to gain information on the yields of each processing step. The percentages of activity left from the original activity after each processing step are shown in Fig. 3. The figure shows also the approximate time spent for each processing step. A major loss in activity happens in the centrifugation step where the submicrometer-sized particles are separated from the initial particle dispersion containing the entire milled batch. As the implanted ions are located mainly in the first few layers of the THCPSi film, considerable loss of activity was expected since nanoparticles can be formed from the entire thickness of the film. The use of relatively thick porous films however facilitated easier and safer mounting and handling of the material at all stages. In the coating processes the yields were about 22% and 18% for THCPSi-RBC and THCPSi-SL-RBC, respectively. Considering this, the final yield of the process, without the split of the activity before the coating procedures to two batches, would be of the order of 1.2–1.5% from the original implanted activity. For this reason, further effort must be made for optimizing the particle processing in order to obtain a higher number of particles of the desired size distribution and minimize loss of the radioactivity. It can also be estimated that due to the relatively large amount of inactive THCPSi film added to the process, only about 0.5% of the produced nanoparticles had a radioactive label. Nevertheless, the particle number and activity obtained were satisfactory for going forward with the biological evaluation.

Characterization of the porous structure was done with the non-radioactive reference nanoparticles, which showed the specific surface area being approximately 242 ± 3 m^2/g with a total pore volume of 0.73 ± 0.02 cm^3/g. These correspond to an average pore diameter of *ca.* 12 nm assuming the pores to be cylindrical. The size and surface properties of the nanoparticles were followed over the coating processes. Table 1 shows the progressive change in the particle size from approximately 160 nm to 200–360 nm determined by dynamic light scattering (DLS) and surface zeta potential after the coatings using the inactive reference THCPSi-RBC and THCPSi-SL-RBC nanoparticles.

A high-angle annular dark-field image of a bare THCPSi nanoparticle and a TEM image of an inactive RBC-THCPSi reference particle are shown in Fig. 4. The RBC membrane does cover the THCPSi particle only partly. The patchy appearance of the RBC membrane coating is likely due to the preferential arrangement of the RBC membrane on the hydrophobic THCPSi surface with the lipophilic layer facing the nanoparticle minimizing the surface water layer between the particle and the membrane. Nevertheless, the coverage was sufficient to improve the stability of the nanoparticle dispersion in physiological media.

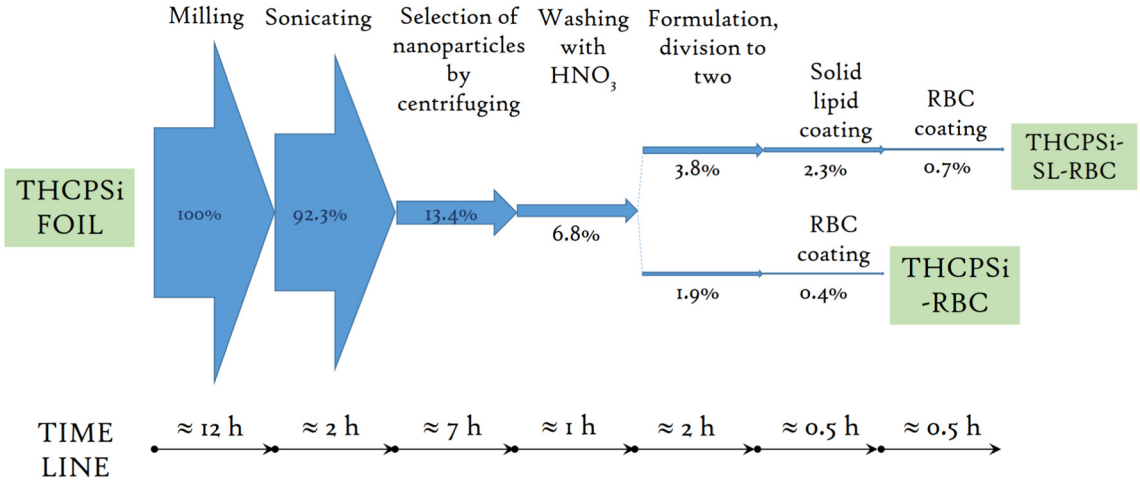

Fig. 3. Processing yields and the time line in the preparation of coated THCPSi nanoparticles from ^{155}Tb-implanted THCPSi films. The main loss of radioactivity in the process is during the selection of the appropriately sized fraction of the nanoparticles.

Table 1
The hydrodynamic diameter, polydispersity index (PdI) and zeta-potential for non-radioactive THCPSi, THCPSi-RBC and THCPSi-SL-RBC particles prepared using semi-permeable membranes with 400-nm and 800-nm pore diameters in the extrusion procedure. The values denote the average ± SD of triplicate measurements. The 400-nm semi-permeable membrane was chosen for the [^{155}Tb]THCPSi-RBC nanoparticle fabrication due to the smaller particle size and lower polydispersity index achieved.

Sample	Semi-permeable membrane pore diameter (nm)	Hydrodynamic diameter (nm)	PdI	ζ-Potential (mV)
THCPSi	–	163 ± 2	0.13 ± 0.02	−19.0 ± 0.5
THCPSi-RBC	400	194 ± 1	0.10 ± 0.01	−10.1 ± 0.7
THCPSi-RBC	800	217 ± 3	0.12 ± 0.01	−9.8 ± 0.3
THCPSi-SL-RBC	400	282 ± 2	0.24 ± 0.01	−16.9 ± 0.4
THCPSi-SL-RBC	800	360 ± 2	0.32 ± 0.04	−21.4 ± 1.1

3.3. In vitro radiolabel stability in physiological media

The *in vitro* radiolabel dissolution test results are shown in Fig. 5 a–c. The radiolabel stability on the particles in physiological media was followed up to 9.5 days. There are no dramatic differences between the radiolabel dissolution properties of the different particles. About 20% of the radioactivity is released until the 60 h measurement point with all the particles in all the solutions. In general, the layers of coating seem to improve the stability of the particles. This can be seen especially in the bare buffer solutions. The particles in plasma were followed up to 60 h and no significant differences between the dissolution of the free radiolabel from the different particle types were observed. Since 10-kDa filters were utilized for separation of the particles from plasma, it cannot be completely ruled out that the larger plasma proteins together with possible protein bound radiometals could have been filtered out together with the particles. Regardless of the coating type, the dissolution results in plasma are in good accordance with the results in buffer solutions, indicating minor contribution of the possible plasma protein binding to the results. Since no significant differences were seen between the THCPSi-RBC and THCPSi-SL-RBC nanoparticles in the *in vitro* radiolabel stability assay, we decided to omit the solid lipid coating and use the [^{155}Tb]THCPSi-RBC particles in the *in vivo* studies. The omission of the solid lipid coating step allowed us to attain higher specific activity (based on the decrease in processing time) as well as smaller size for the injected nanoparticles. The specific activity of the final formulation of [^{155}Tb]THCPSi-RBC used in the intravenous injections was 46.6 ± 0.6 kBq/g.

3.4. In vivo studies: circulation half-life and biodistribution after intravenous delivery

The [^{155}Tb]THCPSi-RBC nanoparticles were well tolerated after a single intravenous administration to female Balb/c mice. The percentage of the injected dose per gram remaining in the blood at given time points is presented in Fig. 6. The RBC membrane coating significantly prolonged the circulation half-life ($t_{c,1/2}$) of THCPSi nanoparticles ($t_{1/2}$ = 42 ± 5 min) when compared to both uncoated ^{18}F-radiolabeled THCPSi [54] and THCPSi-SL [53] nanoparticles (both exhibiting a blood half-life of <5 min). The prolonged persistence of the [^{155}Tb]THCPSi-RBC particles in circulation demonstrates that the RBC membrane coating is able to mask the THCPSi nanoparticles from opsonization and rapid sequestration from the circulation to the organs of the reticulo-endothelial system (RES), the liver and spleen [55]. Interestingly, the circulating nanoparticles could also be subject to selective uptake by the circulating Ly-6C^{high} monocytes as has been shown to other nanomaterials [56], and this could be further investigated as a strategy towards efficient tumor targeting. As non-tumor-bearing mice were used in the pilot study reported herein, the degree of tumor accumulation was not studied.

The *ex vivo* biodistribution after intravenous administration showed pronounced accumulation of [^{155}Tb]THCPSi-RBC to the spleen and the liver (Fig. 7), with slightly elevated radioactivity levels present in the lung (3.8%ID/g) and gall bladder (7.9%ID/g). The interendothelial slits (IES) in the spleen are responsible for the mechanical removal of erythrocytes at the end of their normal lifespan of approximately 120 d, by which the aged, deformed or rigid cells are not able to fit through the narrow gaps in the IES anymore [57,58]. Consequently, it is unsurprising that the RBC membranes harboring a rigid, approximately 200-nm THCPSi nanoparticle are retained in the spleen. This could be avoided by further selecting a THCPSi fraction of <100 nm in diameter for future studies, but it might be challenging to achieve using the top-down production method described. The liver, in turn, removes nanomaterials from the body by the activity of the tissue-resident macrophages, and additionally recycles the iron from disposed erythrocytes [59]. Therefore, nanoparticle accumulation to the liver was also expected. The slightly elevated radioactivity in the gall bladder might result from the degradation of the [^{155}Tb]THCPSi-RBC in the liver and subsequent release of ^{155}Tb, but the radioactive species was not characterized further at this time. Accumulation of radioactivity to the lung and bone (collected with bone marrow) can likely be attributed to nanoparticle aggregation and physical retention in the lung capillaries, and uptake of released ^{155}Tb – a trivalent cation – to the bone [60], respectively.

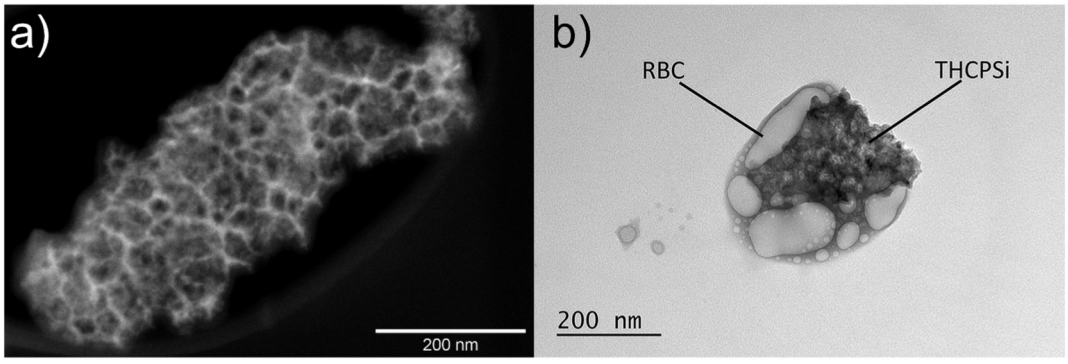

Fig. 4. Micrsocopic images of THCPSi nanoparticles before and after RBC membrane coating. a) High-angle annular dark-field image of a THCPSi nanoparticle b) A representative high-resolution TEM image of a THCPSi-RBC particle showing the RBC membrane layer on the hydrophobic THCPSi surface.

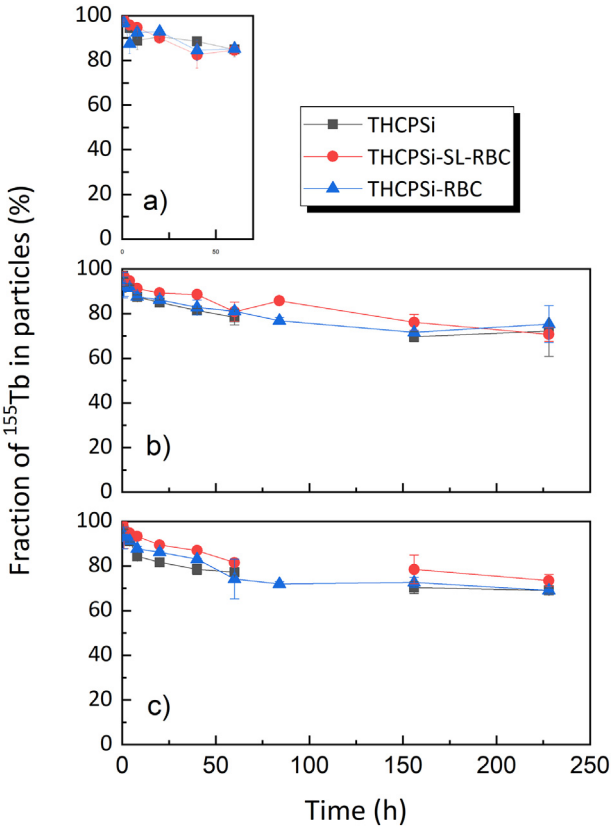

Fig. 5. Results of the *in vitro* dissolution study. The activity remaining in the particles as a function of the incubation time in a) 50% of human plasma and 50% PBS buffer solution of pH 7.4, b) in PBS buffer solution with pH 5.6 and c) in PBS buffer solution with pH 7.4. The samples in plasma were followed up to 60 h and the samples in the buffer solutions up to 228 h. The time point of 84 h is excluded from part of the samples due to an error in the sampling.

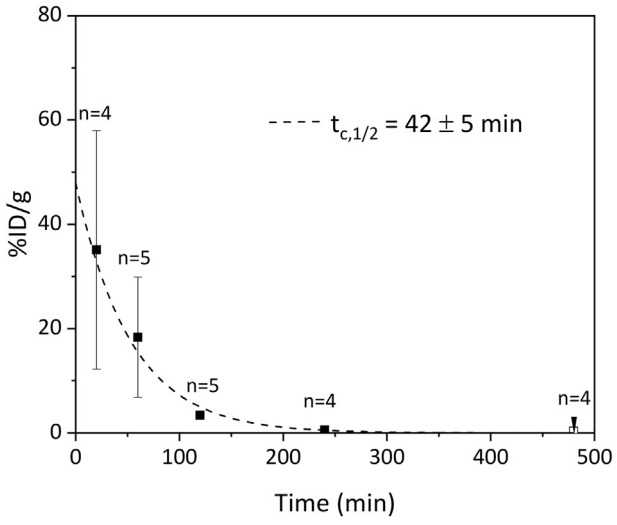

Fig. 6. The measured activity concentrations (%ID/g) in blood as a function of time. The activity concentration is calculated as an average ± SD from the samples of 4–5 mice. The uncertainties are not visible in 3rd and 4th data points are since they are smaller than the marker. The last point (t = 480 min) represents the highest possible value of the average activity at that time point since of one of the samples was already below the minimum detectable activity of the measurement (MDA), and the MDA was used in calculating the average activity. The dashed line is an exponential decay function fitted to the experimental data, resulting in the blood circulation half-life ($t_{c,1/2}$).

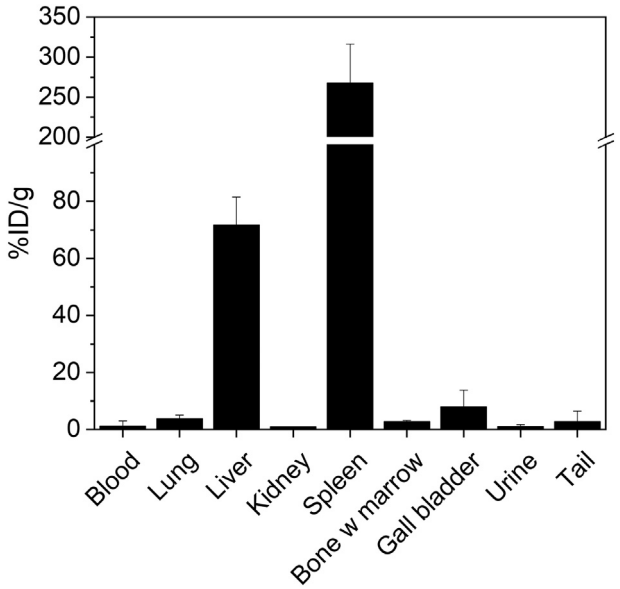

Fig. 7. *Ex vivo* biodistribution of [^{155}Tb]THCPSi-RBC nanoparticles 8 h after a single intravenous injection (9.5 kBq) in Balb/c mice shows a pronounced accumulation of the nanoparticles to the spleen (267.8 %ID/g) and less to the liver (71.7 %ID/g). Columns represent mean ± SD (n = 5).

In a clinical setting the ^{155}Tb release and consecutive bone accumulation would be high with respect to collateral dose to bone marrow. Therefore, methods for improved coating of the particles for the persistence of the radioactive label need to be considered when developing the process further.

4. Conclusions

We have demonstrated using ^{155}Tb RIB-implanted porous silicon nanoparticles coated with mouse RBC membranes the feasibility of using such theranostic nanosystem for the delivery of RIB based radionuclides for radiotherapy with prolonged circulation time. Furthermore, the capability to deliver poorly soluble and sensitive pharmaceutical payloads such as chemotherapeutics and radiosensitizers when trapped in the porous network of PSi opens an interesting avenue for the development of synergistic radiotherapeutic and chemotherapeutic drug delivery systems in the future. Future studies should concentrate on further reducing and refining the size distribution of the nanoparticles obtained, the recovery of the radiolabeled nanoparticles to maximize the specific activity, and translation of the promising nanosystem to therapeutic studies in preclinical cancer models with other RIB based therapeutic isotopes (*e.g.* those of the Tb theranostic quadruplet) and tumor-targeting moieties attached to the RBC membrane coating.

Abbreviations

RIB	Radioactive ion beam
HPGe	High-purity germanium
PEG	Polyethylene glycol
PSi	Porous silicon
RBC	Red blood cell
SEM	Scanning electron microscope
SL	Solid lipid
STEM	Scanning transmission electron microscope
TEM	Transmission electron microscope
THCPSi	Thermally hyrdocarbonized porous silicon

Acknowledgements

This work has been supported by the Academy of Finland (grant numbers 308122, 277190, 298481 and 277423, 278056), the European Union's Horizon 2020 Framework research and innovation programme under grant agreement no. 654002 (ENSAR2) and the University of Helsinki. Prof. H. A. Santos acknowledges financial support from the HiLIFE Research Funds and the Sigrid Jusélius Foundation. We thank the local group at CERN ISOLDE and the IS528 collaboration for the technical support during the implantations.

Appendix A. Supplementary data

Supplementary data to this article can be found online at https://doi.org/10.1016/j.nucmedbio.2020.04.001.

References

[1] Wang C-F, Sarparanta MP, Mäkilä EM, Hyvönen MLK, Laakkonen PM, Salonen JJ, et al. Multifunctional porous silicon nanoparticles for cancer theranostics. Biomaterials 2015;48:108–18.
[2] Riikonen J, Mäkilä E, Salonen J, Lehto V-P. Determination of the physical state of drug molecules in mesoporous silicon with different surface chemistries. Langmuir 2009;25:6137–42.
[3] Santos HA, Bimbo LM, Lehto V-P, Airaksinen AJ, Salonen J, Hirvonen J. Multifunctional porous silicon for therapeutic drug delivery and imaging. Curr Drug Discov Technol 2011;8:228–49.
[4] Kaukonen AM, Laitinen L, Salonen J, Tuura J, Heikkilä T, Limnell T, et al. Enhanced in vitro permeation of furosemide loaded into thermally carbonized mesoporous silicon (TCPSi) microparticles. Eur J Pharm Biopharm 2007;66:348–56.
[5] Kilpeläinen M, Mönkäre J, Vlasova MA, Riikonen J, Lehto V-P, Salonen J, et al. Nanostructured porous silicon microparticles enable sustained peptide (Melanotan II) delivery. Eur J Pharm Biopharm 2011;77:20–5.
[6] Kilpeläinen M, Riikonen J, Vlasova MA, Huotari A, Lehto VP, Salonen J, et al. In vivo delivery of a peptide, ghrelin antagonist, with mesoporous silicon microparticles. J Control Release 2009;137:166–70.
[7] Martins JP, D'Auria R, Liu D, Fontana F, Ferreira MPA, Correia A, et al. Engineered multifunctional albumin-decorated porous silicon nanoparticles for FcRn translocation of insulin. Small 2018;14:e1800462.
[8] Tanaka T, Mangala LS, Vivas-Mejia PE, Nieves-Alicea R, Mann AP, Mora E, et al. Sustained small interfering RNA delivery by mesoporous silicon particles. Cancer Res 2010;70:3687–96.
[9] Tasciotti E, Liu X, Bhavane R, Plant K, Leonard AD, Price BK, et al. Mesoporous silicon particles as a multistage delivery system for imaging and therapeutic applications. Nat Nanotechnol 2008;3:151–7.
[10] Bimbo LM, Sarparanta M, Santos HA, Airaksinen AJ, Mäkilä E, Laaksonen T, et al. Biocompatibility of thermally Hydrocarbonized porous silicon nanoparticles and their biodistribution in rats. ACS Nano 2010;4:3023–32.
[11] Santos HA, Riikonen J, Salonen J, Mäkilä E, Heikkilä T, Laaksonen T, et al. In vitro cytotoxicity of porous silicon microparticles: effect of the particle concentration, surface chemistry and size. Acta Biomater 2010;6:2721–31.
[12] Park J-H, Gu L, von Maltzahn G, Ruoslahti E, Bhatia SN, Sailor MJ. Biodegradable luminescent porous silicon nanoparticles for in vivo applications. Nat Mater 2009;8:331–6.
[13] Low SP, Williams KA, Canham LT, Voelcker NH. Evaluation of mammalian cell adhesion on surface-modified porous silicon. Biomaterials 2006;27:4538–46.
[14] Anderson SHC, Elliott H, Wallis DJ, Canham LT, Powell JJ. Dissolution of different forms of partially porous silicon wafers under simulated physiological conditions. Phys Status Solidi A 2003;197:331–5.
[15] Canham LT, Reeves CL, Newey JP, Houlton MR, Cox TI, Buriak JM, et al. Derivatized mesoporous silicon with dramatically improved stability in simulated human blood plasma. Adv Mater 1999;11:1505–7.
[16] Canham LT. Routes of formation for porous silicon. In: Canham LT, editor. Handbook of porous silicon. Chamonix, Switzerland: Springer; 2018. p. 3–11.
[17] Salonen J, Kaukonen AM, Hirvonen J, Lehto V-P. Mesoporous silicon in drug delivery applications. J Pharm Sci 2008;97:632–53.
[18] Li W, Liu Z, Fontana F, Ding Y, Liu D, Hirvonen JT, et al. Tailoring porous silicon for biomedical applications: from drug delivery to cancer immunotherapy. Adv Mater 2018;30:e1703740.
[19] Shabir Q, Webb K, Nadarassan DK, Loni A, Canham LT, Terracciano M, et al. Quantification and reduction of the residual chemical reactivity of passivated biodegradable porous silicon for drug delivery applications. Silicon 2017;10:349–59.
[20] Sarparanta MP, Bimbo LM, Mäkilä EM, Salonen JJ, Laaksonen PH, Helariutta AMK, et al. The mucoadhesive and gastroretentive properties of hydrophobin-coated porous silicon nanoparticle oral drug delivery systems. Biomaterials 2012;33:3353–62.
[21] Mäkilä E, Ferreira MP, Kivela H, Niemi SM, Correia A, Shahbazi MA, et al. Confinement effects on drugs in thermally hydrocarbonized porous silicon. Langmuir 2014;30:2196–205.
[22] Keinänen O, Mäkilä EM, Lindgren R, Virtanen H, Liljenbäck H, Oikonen V, et al. Pretargeted PET imaging of trans-cyclooctene-modified porous silicon nanoparticles. ACS Omega 2017;2:62–9.
[23] Şen Karaman D, Sarparanta MP, Rosenholm JM, Airaksinen AJ. Multimodality imaging of silica and silicon materials in vivo. Adv Mater 2018;30:e1703651.
[24] Ferreira MP, Ranjan S, Correia AM, Makila EM, Kinnunen SM, Zhang H, et al. In vitro and in vivo assessment of heart-homing porous silicon nanoparticles. Biomaterials 2016;94:93–104.
[25] Janoniene A, Liu Z, Baranauskiene L, Mäkilä E, Ma M, Salonen J, et al. A versatile carbonic anhydrase IX targeting ligand-functionalized porous silicon nanoplatform for dual hypoxia cancer therapy and imaging. ACS Appl Mater Interfaces 2017;9:13976–87.
[26] Joo J, Kwon EJ, Kang J, Skalak M, Anglin EJ, Mann AP, et al. Porous silicon-graphene oxide core-shell nanoparticles for targeted delivery of siRNA to the injured brain. Nanoscale Horiz 2016;1:407–14.
[27] Pap AE, Kordás K, Tóth G, Levoska J, Uusimäki A, Vähäkangas J, et al. Thermal oxidation of porous silicon: study on structure. Appl Phys Lett 2005;86.
[28] Salonen J, Björkqvist M, Laine E, Niinistö L. Stabilization of porous silicon surface by thermal decomposition of acetylene. Appl Surf Sci 2004;225:389–94.
[29] Salonen J, Mäkilä E. Thermally carbonized porous silicon and its recent applications. Adv Mater 2018;30:e1703819.
[30] Mäkilä E, Bimbo LM, Kaasalainen M, Herranz B, Airaksinen AJ, Heinonen M, et al. Amine modification of thermally carbonized porous silicon with silane coupling chemistry. Langmuir 2012;28:14045–54.
[31] Boukherroub R, Wojtyk JTC, Wayner DDM, Lockwood DJ. Thermal hydrosilylation of undecylenic acid with porous silicon. J Electrochem Soc 2002;149:H59–63.
[32] Buriak JM. Illuminating silicon surface hydrosilylation: an unexpected plurality of mechanisms. Chem Mater 2014;26:763–72.
[33] Liu D, Mäkilä E, Zhang H, Herranz B, Kaasalainen M, Kinnari P, et al. Nanostructured porous silicon-solid lipid Nanocomposite: towards enhanced cytocompatibility and stability, reduced cellular association, and prolonged drug release. Adv Funct Mater 2013;23:1893–902.
[34] Rao L, Bu LL, Xu JH, Cai B, Yu GT, Yu X, et al. Red blood cell membrane as a biomimetic nanocoating for prolonged circulation time and reduced accelerated blood clearance. Small 2015;11:6225–36.
[35] Wilhelm S, Tavares AJ, Dai Q, Ohta S, Audet J, Dvorak HF, et al. Analysis of nanoparticle delivery to tumours. Nat Rev Mater 2016;1:16014.
[36] Webster DM, Sundaram P, Byrne ME. Injectable nanomaterials for drug delivery: carriers, targeting moieties, and therapeutics. Eur J Pharm Biopharm 2013;84:1–20.
[37] Fontana F, Fusciello M, Groeneveldt C, Capasso C, Chiaro J, Feola S, et al. Biohybrid vaccines for improved treatment of aggressive melanoma with checkpoint inhibitor. ACS Nano 2019;13:6477–90.
[38] Hu CM, Zhang L, Aryal S, Cheung C, Fang RH, Zhang L. Erythrocyte membrane-camouflaged polymeric nanoparticles as a biomimetic delivery platform. Proc Natl Acad Sci U S A 2011;108:10980–5.
[39] Oldenborg P-A, Zheleznyak A, Fang Y-F, Lagenaur CF, Gresham HD, Lindberg FP. Role of CD47 as a marker of self on red blood cells. Science 2000;288:2051.
[40] Ishida T, Kiwada H. Accelerated blood clearance (ABC) phenomenon upon repeated injection of PEGylated liposomes Special Issue in Honor of Prof Tsuneji Nagai , 354; 2008; 56–62.
[41] Muller C, van der Meulen NP, Benesova M, Schibli R. Therapeutic radiometals beyond (177)Lu and (90)Y: production and application of promising alpha-particle, beta(−)-particle, and Auger electron emitters. J Nucl Med 2017;58 91S–6S.
[42] National Nuclear Data Center, Information extracted from the NuDat 2 database, http://www.nndc.bnl.gov/nudat2/, on 09/19/2019.
[43] Lehenberger S, Barkhausen C, Cohrs S, Fischer E, Grunberg J, Hohn A, et al. The low-energy β^- and electron emitter ^{161}Tb as an alternative to ^{177}Lu for targeted radionuclide therapy. Nucl Med Bio 2011;38:917–24.
[44] Gracheva N, Muller C, Talip Z, Heinitz S, Koster U, Zeevaart JR, et al. Production and characterization of no-carrier-added ^{161}Tb as an alternative to the clinically-applied ^{177}Lu for radionuclide therapy. EJNMMI Radiopharm Chem 2019;4:12.
[45] Müller C, Zhernosekov K, Köster U, Johnston K, Dorrer H, Hohn A, et al. A unique matched quadruplet of terbium radioisotopes for PET and SPECT and for α- and β^--radionuclide therapy: an in vivo proof-of-concept study with a new receptor-targeted folate derivative. 2012;53:1951–9.
[46] dos Santos Augusto R, Buehler L, Lawson Z, Marzari S, Stachura M, Stora T, et al. CERN-MEDICIS (medical isotopes collected from ISOLDE): a new facility. Applied Sciences 2014;4:265–81.
[47] Köster U, Assmann W, Bacri C-O, Faestermann T, Garrett P, Gernhäuser R, et al. Electromagnetic isotope separation of gadolinium isotopes for the production of ^{152,155}Tb for radiopharmaceutical applications. Nucl Instrum Methods Phys Res, Sect B 2020;463:111–4.
[48] Jakobsson U, Mäkilä E, Airaksinen AJ, Alanen O, Etilé A, Köster U, et al. Porous silicon as a platform for radiation theranostics together with a novel RIB-based radiolanthanoid. Contrast Media Mol Imaging 2019;2019:1–9. https://doi.org/10.1155/2019/3728563 Article ID 3728563.
[49] Kugler E, Fiander D, Johnson B, Haas H, Przewloka A, Ravn HL, et al. The new CERN-ISOLDE on-line mass-separator facility at the PS-Booster. Nucl Instrum Methods Phys Res, Sect B 1992;70:41–9.
[50] Köster U, Fedoseyev VN, Mishin VI. Resonant laser ionization of radioactive atoms. Spectrochim Acta B At Spectrosc 2003;58:1047–68.
[51] Rothe S, Marsh BA, Mattolat C, Fedosseev VN, Wendt K. A complementary laser system for ISOLDE RILIS. J Phys Conf Ser 2011;312.
[52] Ziegler JF, Ziegler MD, Biersack JP. SRIM – the stopping and range of ions in matter (2010). Nucl Instrum Methods Phys Res, Sect B 2010;268:1818–23.

[53] Kallinen AM, Sarparanta MP, Liu D, Mäkilä EM, Salonen JJ, Hirvonen JT, et al. In vivo evaluation of porous silicon and porous silicon solid lipid nanocomposites for passive targeting and imaging. Mol Pharm 2014;11:2876–86.
[54] Sarparanta M, Bimbo LM, Rytkonen J, Mäkilä E, Laaksonen TJ, Laaksonen P, et al. Intravenous delivery of Hydrophobin-functionalized porous silicon nanoparticles: stability, plasma protein adsorption and biodistribution. Mol Pharm 2012; 9:654–63.
[55] Bertrand N and Leroux J-C. The journey of a drug-carrier in the body: an anatomo-physiological perspective. J Control Release;161:152–63.
[56] Smith BR, Ghosn EE, Rallapalli H, Prescher JA, Larson T, Herzenberg LA, et al. Selective uptake of single-walled carbon nanotubes by circulating monocytes for enhanced tumour delivery. Nat Nanotechnol 2014;9:481–7.
[57] Drenckhahn D. Removal of old and abnormal red blood cells from circulation: mechanical and immunologic mechanisms. In: Platt D, editor. Blood cells, rheology, and aging. Berlin, Heidelberg: Springer Berlin Heidelberg; 1988. p. 62–72.
[58] Li H, Lu L, Li X, Buffet PA, Dao M, Karniadakis GE, et al. Mechanics of diseased red blood cells in human spleen and consequences for hereditary blood disorders. Proc Natl Acad Sci U S A 2018;115:9574.
[59] Theurl I, Hilgendorf I, Nairz M, Tymoszuk P, Haschka D, Asshoff M, et al. On-demand erythrocyte disposal and iron recycling requires transient macrophages in the liver. Nat Med 2016;22:945.
[60] Carroll V, Demoin DW, Hoffman TJ, Jurisson SS. Inorganic chemistry in nuclear imaging and radiotherapy: current and future directions. Radiochima Acta 2012;100: 653–67.